

RESEARCH ARTICLE | JUNE 20 2024

Separated striations in n-type Czochralski silicon solar cells



Guixiu Li; Shuai Yuan ; Shenglang Zhou; Yihua Wu; Hongrong Chen; Huali Zhang; Chen Wang; Lei Wang; Xuegong Yu ; Deren Yang



Appl. Phys. Lett. 124, 252103 (2024)

<https://doi.org/10.1063/5.0204270>



View
Online



Export
Citation

Applied Physics Letters

Special Topic: Mid and Long Wavelength
Infrared Photonics, Materials, and Devices

Submit Today

Separated striations in n-type Czochralski silicon solar cells

Cite as: Appl. Phys. Lett. **124**, 252103 (2024); doi: [10.1063/5.0204270](https://doi.org/10.1063/5.0204270)

Submitted: 21 February 2024 · Accepted: 11 June 2024 ·

Published Online: 20 June 2024



View Online



Export Citation



CrossMark

Guixiu Li,^{1,2} Shuai Yuan,^{1,2,a)}  Shenglang Zhou,³ Yihua Wu,³ Hongrong Chen,³ Huali Zhang,³ Chen Wang,³ Lei Wang,¹ Xuegong Yu,^{1,a)}  and Deren Yang^{1,2} 

AFFILIATIONS

¹State Key Laboratory of Silicon and Advanced Semiconductor Materials and School of Materials Science and Engineering, Zhejiang University, Hangzhou 310027, People's Republic of China

²Shangyu Institute of Semiconductor Materials, Shaoxing 312300, People's Republic of China

³Jiangsu GCL Silicon Material Technology Development Co., Ltd, Xuzhou 221000, People's Republic of China

^{a)}Authors to whom correspondence should be addressed: shuaiyuan@zju.edu.cn and yuxuegong@zju.edu.cn

ABSTRACT

Currently, in the photovoltaic industry, the market share of n-type monocrystalline silicon is rapidly increasing. However, during mass production, striation defects characterized by concentric circles significantly impact the efficiency of solar cells. In this paper, we investigate the properties and origins of striations in n-type Czochralski silicon solar cells. These striations, occurring in wafers with an oxygen concentration below $7 \times 10^{17} \text{ cm}^{-3}$, are shown to potentially cause an efficiency degradation up to 0.86% absolute. Through an array of techniques, including photoluminescence, optical microscopy (OM), electron beam induced current (EBIC), and Fourier Transform Infrared Spectroscopy, this work demonstrates that such defects primarily form after the thermal treatment processes in the manufacturing of solar cells and indirectly proves that these defects are related to the precipitation behavior of oxygen. Notably, traditional methods of post-polishing and etching followed by OM and EBIC technique failed to detect these defects. Therefore, the indirect characterization methods designed in this study hold significant referential value.

Published under an exclusive license by AIP Publishing. <https://doi.org/10.1063/5.0204270>

Owing to the absence of boron-oxygen complexes and reduced sensitivity to metal impurities,¹ n-type Czochralski silicon (Cz-Si) solar cells exhibit promising potential for achieving high efficiencies. Projections indicate an anticipated growth in their photovoltaic (PV) market share, reaching approximately 65% by 2033.² Presently, the Tunnel Oxide Passivated Contact (TOPCon) technique is prevalently employed in n-type solar cells.³ However, n-type TOPCon cells necessitate a higher thermal budget compared to p-type Passivated Emitter Rear Cells (PERCs), occasionally leading to the formation of striations during high-temperature processing. These striations, characterized by a dark core or concentric rings of low carrier lifetime regions in photoluminescence (PL) measurements, adversely impact the efficiency of n-type solar cells. Prior research links the formation of striations, especially those with a dark core in cells with elevated interstitial oxygen concentrations ($[O_i]$), to oxygen precipitations (OPs),^{4,5} potentially causing more than a 4% absolute efficiency loss.⁴⁻⁶ Le Donne *et al.*⁷ observed an emission band at 0.87 eV in the striation regions of the top solar cell precursors through PL measurements taken at 110 K. In addition, Zhou *et al.*⁸ discovered a dark center in n-type Cz-Si wafers

subjected to the polysilicon contact process, with PL spectra of these dark striations measured at 80 K revealing emission peaks at 0.87, 0.94, and 1.04 eV. These striations are also associated with energy levels extracted as $E_v + 0.33 \text{ eV}$ in deep level transient spectroscopy (DLTS) spectra.⁵ All of them attributed these energy levels to oxygen precipitates by comparing the results with previous literature works. Hence, the control of oxygen content to avoid the formation of oxygen precipitations is crucial for manufacturing efficient solar cells. Despite reductions in $[O_i]$ in n-type Cz-Si to below $7 \times 10^{17} \text{ cm}^{-3}$, striations persist, now appearing as fine-lined concentric rings. The underlying mechanisms and properties of these striations are not yet fully understood. Understanding and mitigating such striation-related issues are crucial for the advancement of high-efficiency solar cell production. This study aims to meticulously investigate the impact of these striations on solar cell performance and to elucidate their formation mechanisms, with a focus on fine-lined concentric ring striations.

In this study, a batch of commercially standard, phosphorus-doped n-type, industrial-scale Czochralski silicon (Cz-Si) wafers were randomly selected from GCL Co., Ltd. Utilizing these samples, 300,000

TABLE I. Ranges of material parameters for the sample set.

Ingot number	Ingot type	Number	ρ ($\Omega\cdot\text{cm}$)	$[\text{O}_i]$ ($\times 10^{17} \text{ cm}^{-3}$)	$[\text{C}_s]$ ($\times 10^{17} \text{ cm}^{-3}$)
1	n-Type	11	0.3–1.1	5.4–6.3	0.2–1.3
2	n-Type	11	0.5–1.3	4.5–5.6	0.1–0.5
3	n-Type	12	0.5–1.2	4.4–6.7	0.1–2.0

n-type Tunnel Oxide Passivated Contact (TOPCon) solar cells, each measuring $182 \times 182 \text{ mm}^2$, were produced employing a standard industrial solar cell process by GCL. For the fabrication of these solar cells, wafers underwent alkaline texturing to create pyramid structures. This was followed by cleaning and a boron diffusion process conducted in a tubular furnace at temperatures ranging from 850 to 1030°C . Subsequently, a tunnel oxide layer was developed on the rear side of the wafers. Over this layer, phosphorus-doped polysilicon was deposited. Surface passivation with silicon nitride was then applied to both sides using plasma-enhanced chemical vapor deposition (PECVD). The final steps involved screen printing and co-firing to establish metal contacts.

The completed solar cells underwent testing to ascertain their characteristic parameters, with striations being identified via photoluminescence (PL) imaging to examine the effect of striations on cell performance. Furthermore, 34 wafers were selected from the head, middle, and tail of three ingots for detailed characterization to explore the formation mechanism of striations more thoroughly. Specifications of these wafers, such as resistivity, interstitial oxygen concentration ($[\text{O}_i]$), and substitutional carbon concentrations ($[\text{C}_s]$), are detailed in Table I. These wafers underwent photoluminescence (PL) imaging both before and after a diffusion-treated annealing process (referred to as TA1) to examine the effect of thermal treatment during the boron diffusion process, as illustrated in Fig. 1(a). For more in-depth examination, a defective wafer underwent further annealing at 1050°C for 16 h in an argon atmosphere, commencing at 600°C with a heating rate of $1^\circ\text{C}/\text{min}$ ^{9–11} [referred to as TA2, illustrated in Fig. 1(b)]. This procedure was designed to promote the growth of existing oxygen precipitations (OPs) in the samples. The $[\text{O}_i]$ s were measured using a Bruker VERTEX 70v Fourier Transform Infrared Spectroscopy (FTIR) spectrometer both before and after the etch step annealing process. Measurements were conducted in accordance with

the ASTM F121-83 standard, applying a calibration coefficient of $3.14 \times 10^{17} \text{ cm}^{-2}$ at room temperature. The FTIR measurement was calibrated with a Secondary Ion Mass Spectrum (SIMS) measurement, using a randomly selected sample. The results were FTIR: $5.68 \times 10^{17} \text{ cm}^{-3}$ and SIMS: $5.74 \times 10^{17} \text{ cm}^{-3}$, which suggested that the major form of oxygen in as-cut wafer should be interstitial state. Subsequently, an optical microscope (OM) and an electron beam induced current (EBIC) technique were employed to examine micro-defects post-TA1 and post-TA2, respectively. The OM analysis followed a 10-min etching process using the Yang1 solution [$\text{V}(\text{CrO}_3, 0.5 \text{ mol/L}; \text{V}(\text{HF } 49\%) = 1:1]$].

Figure 2(a) displays the photoluminescence (PL) imagery of a defective solar cell characterized by striations, which appear as dark fine-lined concentric rings indicative of heightened recombination activity. By comparing the average performance of cell slices from the same batch in large-scale experiments, information on the quality differences between groups of silicon wafers can be obtained from the low signal-to-noise ratio of cell performance data. In this work, a total of 300,000 cells were statistically analyzed from the production line. Through determining the contrast threshold values in electroluminescence (EL) imaging, the concentric-circle defective group and the non-defective group (referential group) were identified. Defective samples are identified through EL imaging, where samples with a striations' intensity below 70% of the normal value are classified as defective. A comparison of the cell performance between these two groups was then conducted as shown in Table II. The defective cells constitute approximately 1.35% of the entire batch. Their efficiency is notably lower, by 0.86%, compared to the referential cells. Table III displays a smaller batch of data, selecting performance differences between a closely numbered set of defective and referential cells. The defective wafers exhibit lower values in open-circuit voltage (V_{OC}) and fill factor (FF) and also show greater variability. These are typical characteristics

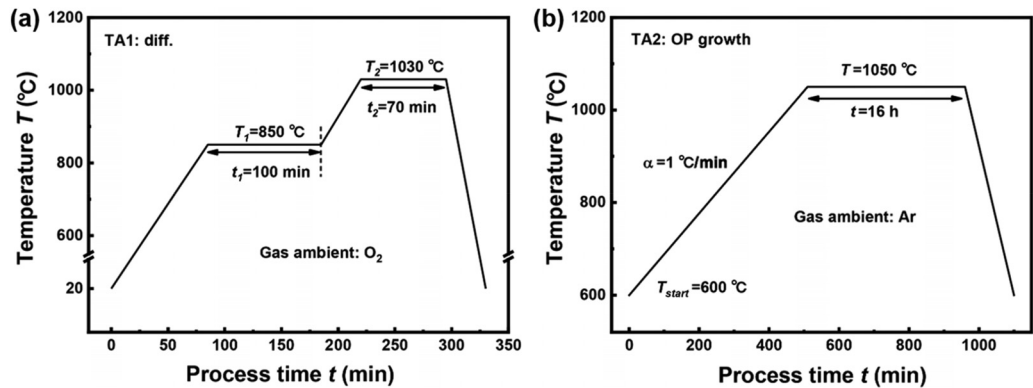


FIG. 1. Schematic representation of temperature–time profiles for the TA1 process (a) and TA2 process (b).

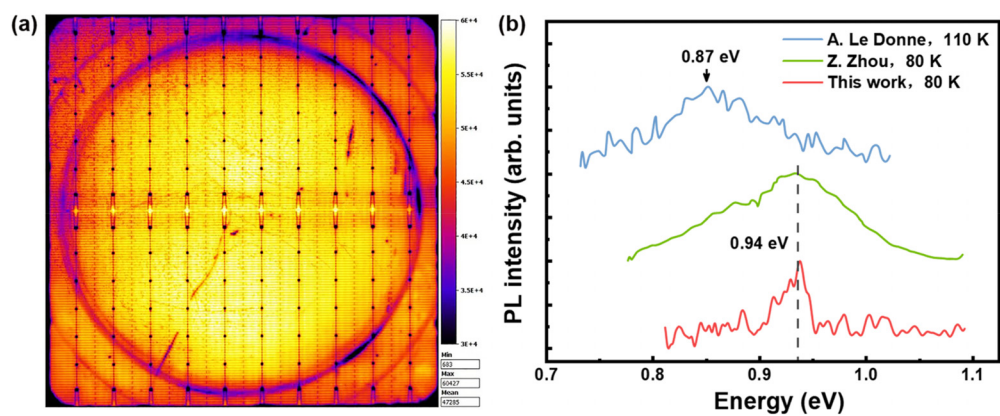


FIG. 2. (a) The PL image of a defective cell with the striations. (b) A PL spectrum of the striation regions measured at 80 K and compared with the results of the previous works.^{7,8}

TABLE II. Average solar cell performance of the industrial set (300,000 cells, 13 October 2023).

Samples	Ratio (%)	V_{oc} (mV)	I_{sc} (A)	FF (%)	$Eff.$ (%)
Defective	1.35	713.4	13.60	84.01	24.47
Referential	98.65	721.1	13.68	84.82	25.33

of silicon wafers with recombination-active defects. Compared to Table II, the cell efficiency in Table III has significantly improved, yet the performance differences between the two groups remain substantial, highlighting the importance of addressing the defect issues.

The PL spectrum of the striations, measured at 80 K, reveals a distinctive radiative emission energy at 0.94 eV, as illustrated in Fig. 2(b). Previous studies^{12,13} have established that both dislocations and oxygen precipitations (OPs) typically exhibit optical emissions in the 0.8–1.0 eV range. Crucially, in our analysis, the notable absence of the D1 emission band (0.807 eV)—commonly acknowledged as a PL signature of dislocation presence—enables us to rule out dislocations as a contributing factor. Therefore, we attribute the emission at 0.94 eV observed in our study primarily to OPs. Additionally, the emission energy level of the striations in our research is analogous to those of striations in dark core reported in Ref. 8 but different from those in Ref. 7, with all these defect bands purportedly associated with oxygen precipitations. We speculate that the difference of defect energy level is related to the morphology of oxygen precipitation.^{12,13} The difference between Refs. 7 and 8 is that the oxygen concentration in Ref. 7 is notably elevated, peaking at $9 \times 10^{17} \text{ cm}^{-3}$, resulting in the formation of larger and more complicated morphology of oxygen precipitates¹⁴ post-diffusion, thus contributing to a deeper Fermi energy level of defect.

TABLE III. Solar cell performance of a small industrial batch (~400 cells, 21 March 2024).

Samples	Number	V_{oc} (mV)	I_{sc} (A)	FF (%)	$Eff.$ (%)
Defective	215	733.4 ± 3.93	13.84 ± 0.02	84.99 ± 1.23	25.90 ± 0.48
Referential	189	736.4 ± 0.78	13.83 ± 0.01	85.79 ± 0.21	26.23 ± 0.08

Further experiments were conducted on wafers to investigate the genesis of striations in solar cells. PL imaging of all as-grown wafers, as referenced in Table I, revealed the absence of striations. After the TA1 process, these wafers were classified into two categories: (1) Group A, exhibiting striations, and (2) Group B, devoid of them. Figure 3(a) depicts the PL images of these groups both in their as-grown state and after undergoing TA1. Due to the dopant segregation effect during the growth of Cz-Si, the resistivity changes in a unidirectional manner, allowing the resistivity to reflect the position of the silicon wafer within the crystal. Figure 3(b) illustrates the relationship between the initial oxygen concentration $[O_i]$ of the 34 randomly selected wafers and their resistivity. After undergoing the TA1 thermal treatment, samples that exhibited defects are indicated by blue points, while those without defects are marked with red points. This figure further elucidates that striations occur exclusively in wafers from the head and tail sections of the ingots, where the $[O_i]$ is relatively higher compared to the middle sections. This pattern underscores a direct relationship between oxygen levels and striation formation. Figure 3(c) displays optical microscope (OM) images post-etching and electron beam induced current (EBIC) images of specific areas indicated by blue points in Fig. 3(a2). In these images, no discernible defects were observed in either the regions with or without striations. This indicates that the “conventional methods” used to characterize the chemical and electrical activity of defects are unable to characterize the defects shown by PL mapping. Therefore, we adopted a method that promotes the formation of large-size oxygen precipitates to indirectly observe the difference in the internal defect content of silicon wafers after TA1 treatment. By adding the TA2 heat treatment (1050 °C, 16 h), a sufficiently long heat treatment allows the supersaturated interstitial oxygen to form more and larger observable precipitates. After TA2 process, distinct rod-shaped bulk stacking faults (BSFs) were observed

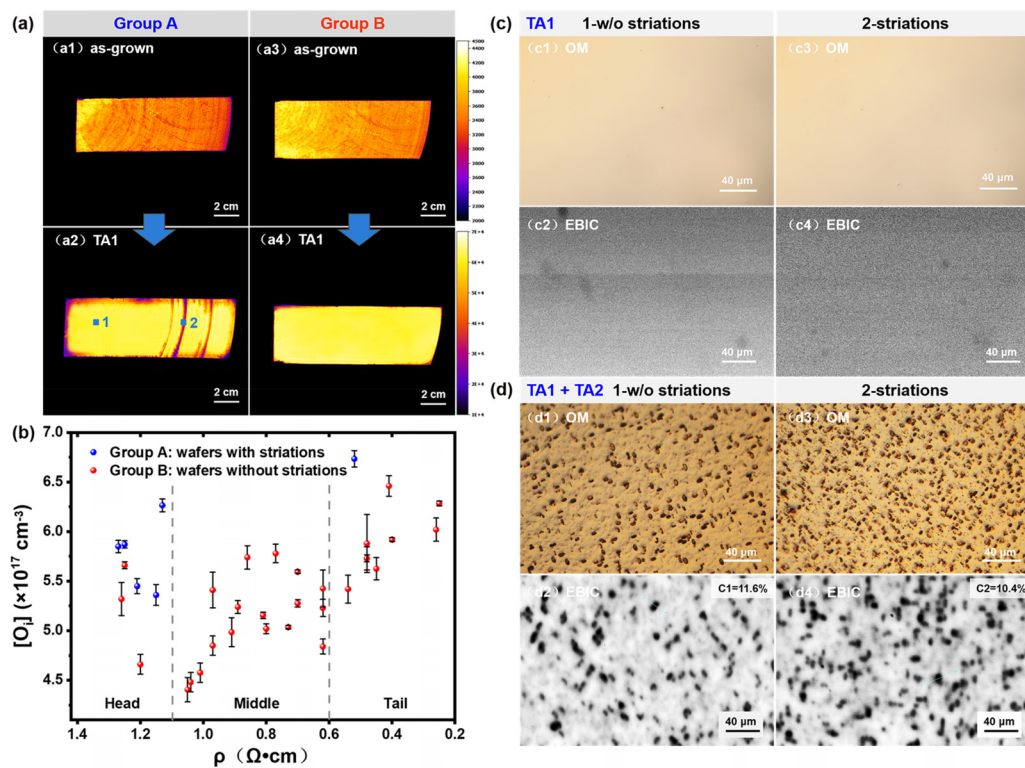


FIG. 3. (a) PL images of the two groups of wafers in the as-grown state and after the TA1. (b) The initial $[O_i]$ and position in the ingot of the two groups of wafers. (c) OM and EBIC images of marked positions (1-w/o striations, 2-striations) after TA1. (d) OM and EBIC images of 1-w/o striations and 2-striations after two-step anneal (TA1 + TA2).

in both OM and EBIC images of the two regions highlighted in Fig. 3(d), where the distribution of BSFs within these two regions exhibits pronounced differences, indicating variability in defect formation dynamics across the different wafer areas.

After the TA2 heat treatment, as depicted in Fig. 4(a), we observed a significantly higher density of bulk stacking faults (BSFs) in the striation region compared to the region without striations. Furthermore, the reduction in interstitial oxygen concentration ($[O_i]$) in the striation region was more pronounced than in the no-striation region after both TA1 and TA1 + TA2 treatments, as shown in Fig. 4(b). This difference suggests a greater presence of as-grown oxygen precipitation (OP) nuclei in the striation areas of the as-grown defective wafer. Considering that high-temperature processes like TA1 and TA2 (ranging from 850 to 1050 °C) are not conducive to the formation of new OP nuclei,¹⁵ it is inferred that the development of striations is associated with the growth of these preexisting OP nuclei into recombination-active OPs during the diffusion process. These OPs are initially so small that they elude detection by etching and EBIC techniques. However, after undergoing the TA2 process, these OPs grow into BSFs, becoming sufficiently large to be detected by both etching and EBIC. Figure 4(c) provides a schematic illustration of the proposed striation formation mechanism.

Additionally, the small areas of position 1 and position 2 marked in Fig. 3(a2) were cleaved with a diamond pen and their cross sections were inspected by OM, as shown in Fig. 5. The OM images of the cross

section are consistent with those on the front surface. In the samples undergoing TA1, no visual defects were observed, whereas, in the samples after TA2 process, the distribution of BSFs is uniform in depth except for the dozens of micrometers of denuded near the surface. Consistent with the front surface observations shown in Fig. 3(d), the striation regions have a significantly higher density of BSFs than the regions without striation. These results suggest that the striations belong to bulk defects of silicon rather than surface defects.

Drawing from the gathered evidence, it can be deduced that the striations observed in this study are attributed to small oxygen precipitations (OPs) that emerge during the diffusion process. Therefore, to effectively mitigate the formation of striations, it is crucial to both reduce the oxygen concentration and refine the diffusion process. One potential strategy to address striation issues involves the application of a magnetic field during the crystal growth of silicon.^{16–18} This approach can help in moderating the formation of oxide nuclei throughout the ingot's growth and subsequent cooling phases. Additionally, subjecting wafers to a thermal treatment at temperatures around 1000 °C before commencing solar cell processing steps is advisable for dissolving as-grown oxygen nuclei.^{19,20} Another viable solution is to optimize the diffusion process in solar cell fabrication by employing a short, high-temperature dwell-time,²¹ which is instrumental in suppressing the growth of OPs.

In conclusion, this study reveals that striations, characterized by fine-lined concentric rings, are occasionally observed on solar cells

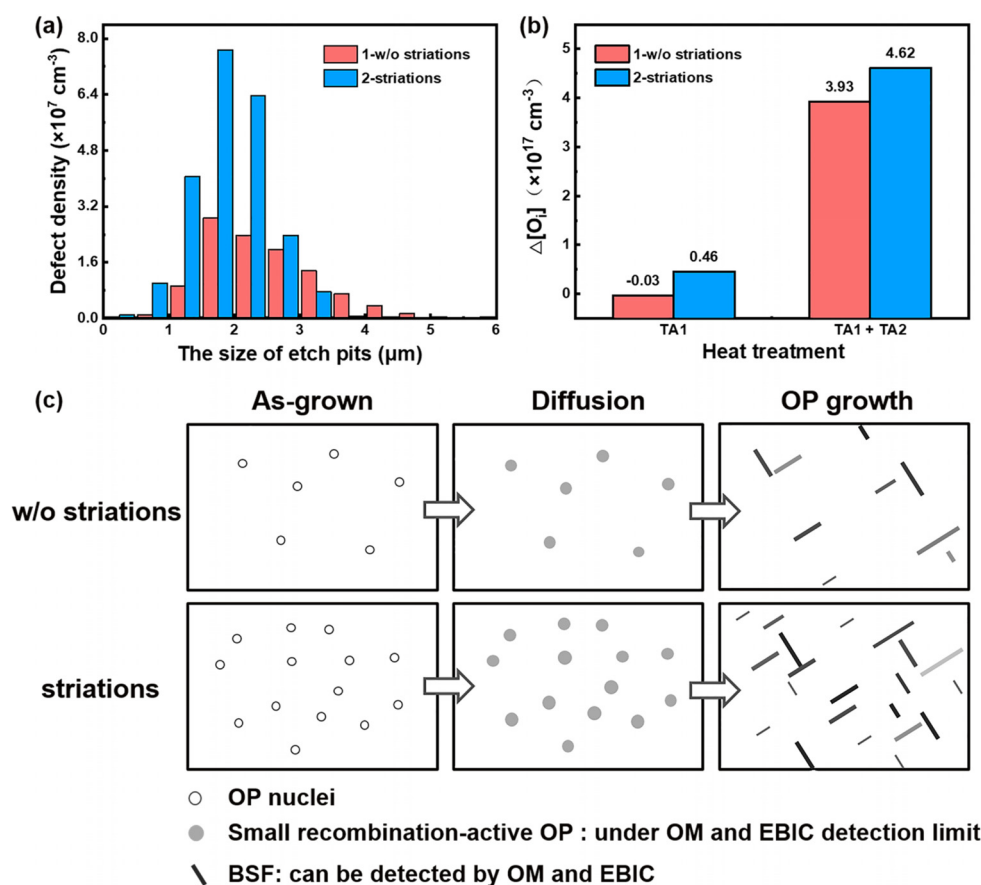


FIG. 4. (a) The distribution of defect density for different defect sizes, respectively, in 1-w/o striations and 2-striations after TA1 + TA2. (b) The loss of $[\text{O}_i]$ in 1-w/o striations and 2-striations after TA1 and TA1 + TA2. (c) Schematic illustration of OP evolution in 1-w/o striations and 2-striations, respectively, in as-grown, TA1 diffusion-treated and TA2 OP growth-treated states.

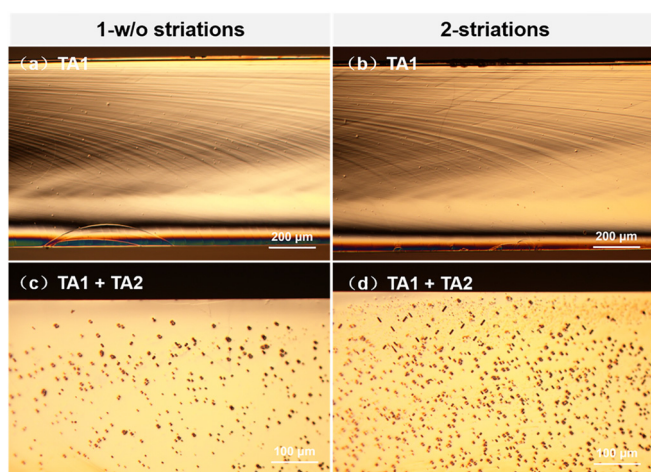


FIG. 5. OM images of Yang1 defect-etched cross sections for the specimens with-out striations and with striations subjected to (a, b) TA1 and (c, d) TA1 + TA2.

manufactured from wafers with an interstitial oxygen concentration below $7 \times 10^{17} \text{ cm}^{-3}$. These striations have been identified as causing up to a 0.86% absolute decrease in solar cell efficiency. Photoluminescence measurements indicate that these striations result in a radiative emission energy at 0.94 eV. Notably, such striations are absent in as-grown wafers but emerge in the head and tail wafers, which have higher $[\text{O}_i]$, following the diffusion-treated TA1 process. Subsequent to the OP growth-treated TA2 annealing process, an increased density of bulk stacking faults (BSFs) and heightened $[\text{O}_i]$ loss in striated regions are evident, suggesting the presence of numerous as-grown OP nuclei. Consequently, our findings demonstrate that a multitude of as-grown OP nuclei in the striation region transform into recombination-active OPs during the solar cell's diffusion process, thereby inducing the observed striation defects.

The authors would like to thank the financial support from the National Natural Science Foundation of China (Nos. 62004173, 62025403, and 61721005), the National Key R&D Program of China (2020YFB1506502), the Natural Science Foundation of

Zhejiang Province (LDQ23E020002), the Fundamental Research Funds for the Central Universities (226-2022-00200), the Open Project of Key Laboratory of Solar Energy Utilization and Energy Saving Technology of Zhejiang Province (ZJS-OP-2020-01), the Key Project of Zhejiang Province (2021C01170), and Jiangsu Provincial Key Laboratory of Silicon-based Electronic Materials.

AUTHOR DECLARATIONS

Conflict of Interest

The authors have no conflicts to disclose.

Author Contributions

Guixiu Li: Conceptualization (equal); Methodology (equal); Formal analysis (equal); Data curation (lead); Visualization (lead); Writing – original draft (lead). **Shuai Yuan:** Conceptualization (equal); Methodology (equal); Formal analysis (equal); Supervision (lead); Project administration (lead); Writing – review & editing (lead); Funding acquisition (lead). **Shenglang Zhou:** Resources (equal); Investigation (equal); Data Curation (supporting). **Yihua Wu:** Resources (equal); Investigation (equal); Data Curation (supporting). **Hongrong Chen:** Resources (equal); Investigation (equal). **Huali Zhang:** Investigation (equal); Project administration (supporting). **Chen Wang:** Investigation (equal); Project administration (supporting). **Lei Wang:** Supervision (supporting); Funding acquisition (supporting). **Xuegong Yu:** Supervision (supporting); Funding acquisition (supporting). **Deren Yang:** Supervision (supporting); Project administration (supporting); Writing – review & editing (supporting); Funding acquisition (supporting).

DATA AVAILABILITY

The data that support the findings of this study are available from the corresponding author upon reasonable request.

REFERENCES

- ¹D. Song, J. Xiong, Z. Hu, G. Li, H. Wang, H. An, B. Yu, B. Grenko, K. Borden, and K. Sauer, *38th IEEE Photovoltaic Specialist Conference* (IEEE, 2012), p. 003004.
- ²See <http://www.itrpv.net/> for international technology roadmap for photovoltaic (ITPRV), 14th ed., April 2023.
- ³D. K. Ghosh, S. Bose, G. Das, S. Acharyya, A. Nandi, S. Mukhopadhyay, and A. Sengupta, *Surf. Interfaces* **30**, 101917 (2022).
- ⁴J. Haunschild, I. E. Reis, J. Geilker, and S. Rein, *Phys. Status Solidi RRL* **5**(5–6), 199 (2011).
- ⁵Z. Wang, X. Zhu, S. Yuan, X. Yu, and D. Yang, *Sol. Energy Mater. Sol. Cells* **236**, 111533 (2022).
- ⁶L. Chen, X. Yu, P. Chen, P. Wang, X. Gu, J. Lu, and D. Yang, *Sol. Energy Mater. Sol. Cells* **95**(11), 3148 (2011).
- ⁷A. Le Donne, S. Binetti, V. Folegatti, and G. Coletti, *Appl. Phys. Lett.* **109**, 033907 (2016).
- ⁸Z. Zhou, F. Rougieux, M. Siriwardhana, and G. Coletti, *Sol. Energy Mater. Sol. Cells* **248**, 111965 (2022).
- ⁹J. Chen, D. Yang, H. Li, X. Ma, and D. Que, *J. Cryst. Growth* **291**(1), 66 (2006).
- ¹⁰Y. Zeng, D. Yang, X. Ma, X. Zhang, L. Lin, and D. Que, *ECS Trans.* **18**(1), 1001 (2009).
- ¹¹P. Wang, C. Cui, X. Yu, and D. Yang, *Mater. Sci. Semicond. Process.* **74**, 369 (2018).
- ¹²S. Binetti, S. Pizzini, E. Leoni, R. Somaschini, A. Castaldini, and A. Cavallini, *J. Appl. Phys.* **92**(5), 2437 (2002).
- ¹³E. Leoni, L. Martinelli, S. Binetti, G. Borionetti, and S. Pizzini, *J. Electrochem. Soc.* **151**(12), G866 (2004).
- ¹⁴H. Fujimori, *J. Electrochem. Soc.* **144**(9), 3180 (1997).
- ¹⁵D. Yang, D. Li, L. Wang, X. Ma, and D. Que, *Sol. Energy Mater. Sol. Cells* **72**(1–4), 133 (2002).
- ¹⁶Z. A. Salnick, *J. Cryst. Growth* **121**(4), 775 (1992).
- ¹⁷K. Hoshikawa, H. Kohda, H. Hirata, and H. Nakanishi, *Jpn. J. Appl. Phys.* **19**(1), L33 (1980).
- ¹⁸X. Yu and D. Yang, *Handbook of Photovoltaic Silicon* (Springer, 2019).
- ¹⁹E. Looney, H. S. Laine, M. A. Jensen, A. Youssef, V. LaSalvia, P. Stradins, and T. Buonassisi, *IEEE 44th Photovoltaic Specialist Conference (PVSC)* (IEEE, 2017), p. 1491.
- ²⁰R. Basnet, S. P. Phang, C. Sun, F. E. Rougieux, and D. Macdonald, *J. Appl. Phys.* **127**(15), 153101 (2020).
- ²¹S. Maus, S. Mack, J. Schön, M. Messmer, A. Wolf, and O. Paul, *Sol. RRL* **7**(4), 2200980 (2023).